Geomechanics for Energy and the Environment 26 (2021) 100233

Contents lists available at ScienceDirect

Geomechanics for Energy and the Environment

journal homepage: www.elsevier.com/locate/gete

Ion-species in pore fluids with opposite effects on limestone fracturing

A. Pluymakers [a,*], A. Ougier-Simonin [b], A. Barnhoorn [a]

[a] Faculty of Civil Engineering & Geosciences, Delft University of Technology, Delft, The Netherlands
[b] Rock Mechanics and Physics Laboratory, British Geological Survey, Nottingham, UK

ARTICLE INFO

Article history:
Received 24 June 2020
Received in revised form 6 January 2021
Accepted 6 January 2021
Available online 9 January 2021

Editors-in-Chief:
Professor Lyesse Laloui and Professor Tomasz Hueckel

Keywords:
Carbonate
Fluid–rock interaction
Rock mechanics
Triaxial testing
$MgSO_4$
Na_2SO_4

ABSTRACT

At ten percent of sedimentary rocks, limestones are common geo-energy reservoirs. Being highly soluble, limestones are prone to fluid-assisted deformation and their mechanical behaviour likely susceptible to fluid chemistry. In this study, we saturated limestone samples with 0.4 M $MgSO_4$ or 0.4 M Na_2SO_4 $CaCO_3$-saturated solutions (naturally present in many reservoirs) or a reference $CaCO_3$-saturated solution for 1, 50 or 200 days prior to mechanical testing. Triaxial deformation tests were then performed at 7, 30, and 70 MPa of confining pressure room temperature, under drained conditions. Our results show that exposure to one different cation impacts the strength of this rock (up to $\frac{1}{2}$ of dry rock strength) and its failure dynamics, associated with different microstructural damage distribution. A 200 day exposure to $MgSO_4$ promotes strengthening whilst similar exposure to Na_2SO_4 leads to weakening. We posit that these strength changes may be related to changes in surface charges on the mineral surfaces. More data on fluid–rock interaction will be key to fully understand fracture propagation in natural carbonate formations.

1. Introduction

Seawater injection in the 1980s to halt the subsidence of the carbonate-rich Ekofisk oil field (North Sea, Norway) led to an additional and dramatic 10 m of subsidence instead.[1] Of the common sedimentary rocks, limestone in particular exhibits fast dissolution, especially at low pressures and temperatures. Dissolution is a process sensitive to pH, salinity, and CO_2 content[2–4] which makes limestones (and other carbonate-rich sedimentary rocks) also sensitive to water-assisted deformation processes during mechanical loading, including time-dependent stress-corrosion microcracking[5] and pressure-enhanced dissolution.[6] Today's knowledge on fluid-assisted rock deformation has improved, but the occasionally dramatic effects of fluid chemistry on deformation behaviour remain underappreciated. This is of particular importance, since there is brine present in all sedimentary basins,[7] with examples of common ions being Na, Ca, Mg, Cl, CO_3, and SO_4.[8] Local equilibrium will depend on local hydrogeology, and changes in flow conditions should affect such an equilibrium. Moreover, several saline limestone aquifers are hydrocarbon reservoirs, wastewater injection sites, geothermal energy reservoirs and potential CO_2 geological storage sites. Reservoir geo-engineering involves manipulating the fluid chemistry on timescales of the order of days to several years, which is short compared to geological timescales of thousands of years. Today's pressure on natural resources and space resulting from world population growth, needs and disparate distribution increasingly drives to a greater usage of the underground. Reservoir stability is paramount since reservoir compaction can lead to severe economic and environmental consequences such as induced seismicity, well failure, and surface subsidence [e.g. Ref. 1]. This highlights the importance of understanding the coupled mechano-chemical effects on the targeted rock. Furthermore, many limestone formations in populated areas (such as the Greek Corinth rift zone, and the Italian Apennines[9]) are also earthquake-prone. In these regions, earthquakes are shown to be regularly correlated to high pressure fluid fluxes,[10–12] with the potential for associated changes in fluid chemistry. There are numerous studies linking induced seismicity to fluid pumping,[13–16] and many others even before taking any potential chemical effects into account.

In limestone, water weakening manifests as reduced peak strength and/or reductions in the stress at the onset of inelastic behaviour.[17–21] Very few studies exist that investigate the combined mechano-chemical effects of brine on limestone deformation, though there are indications that with decreasing water activity carbonate-rich rocks become stronger,[17,19,22] except for Na_2SO_4-rich solutions. In the presence of Na_2SO_4 a decrease in strength and bulk modulus has been observed[23,24] in highly porous limestone rocks tested at elevated temperatures, due to lowering of mineral surface charges.[23] As a known inhibitor to carbonate precipitation and dissolution, Mg^{2+} has been used to

* Corresponding author.
E-mail address: anne.pluymakers@tudelft.nl (A. Pluymakers).

https://doi.org/10.1016/j.gete.2021.100233

slow down pressure-enhanced carbonate dissolution.[25] Finally, at similar water activity, one study has shown that $MgSO_4$ and Na_2SO_4 have opposite effects on crack propagation rates in cm-sized single calcite crystals.[26] Natural reservoir brines are usually a mixture of many ions [e.g.] Ref. 27, and all of these are common ions in subsurface brines,[8] as well as being ions of interest in enhanced oil recovery.[28] If $MgSO_4$ and Na_2SO_4 adversely affect the propagation of a single crack, then what is the net effect on the dynamics of failure of a carbonate-rich sedimentary rock, essentially composed of many calcite crystals? We address this question performing triaxial experiments simulating relevant reservoir pressure conditions on chemically treated limestone samples.

2. Materials and methods

2.1. Materials

Brine solutions were prepared by dissolving in DI water the appropriate quantity of $MgSO_4$ or Na_2SO_4 salt to create a 0.4 M solution. The choice for these solutions and this concentration was motivated by the results of Bergsaker et al.[26] who indicated a large difference between $MgSO_4$ and Na_2SO_4 on the rate of crack growth in a calcite crystal at concentrations in this range. Solutions were stirred until visual confirmation indicated all salt was dissolved, after which excess ground $CaCO_3$ powder (obtained from grinding and sieving leftover pieces of the limestone tested) was added. Subsequently, all solutions were stirred for 48+ hours, the time needed to create a saturated solution.[3,25,29] We then saturated our limestone samples with each solution under vacuum until all air bubbles were gone (indicating full saturation, 2 to 3 h minimum), and samples were tested either the next day (S), or left to sit under room temperature (20 °C; environmentally controlled chamber) and ambient pressure for 50 days (L) or 200 days (XL). During exposure time, the sample container was closed off, and hence contained the fluid, the sample, excess carbonate powder and a fixed (but ample) supply of air. This means that the solutions were in equilibrium with atmospheric CO_2, but no evaporation could take place, thus ensuring the fluid composition remains constant over time. Reference experiments were performed with overnight saturation in $CaCO_3$-saturated solution only. The use of $CaCO_3$-saturated solutions with excess fine-grained powder ensures there was no net dissolution during the waiting time and the experiment, hence no chemical reaction was expected, and the initial sample characteristics (such as mass, porosity) should remain unaffected during the waiting time. Note that the excess ground powder was kept in the solution during this waiting time to ensure continuous saturation by having excess fine-grained material that can easily dissolve and precipitate due to small temperature changes (similar to the procedure used when dissolving a less soluble ionic compound[c.f.] Ref. 30). A geochemical equilibrium batch reaction model (PHREEQC[31]) indicates that a saturated carbonate solution with these concentrations of $MgSO_4$ or Na_2SO_4 have a pH of 8.25; i.e. the presence of the salts does not lead to additional dissolution/precipitation. The exposure duration is expected to affect the diffusion of ion species throughout the pore fluid, especially in the grain boundary fluid, the effect of which is quantified here in terms of influence on mechanical behaviour of the rock samples.

The limestone samples used in this study are from the same dm-sized blocks as used by Castagna et al.[32] These blocks were collected from the Ragusa Formation of the Western Hyblean Plateau, accessed in section via outcrops in a quarry near the Comiso village in southeast Sicily, Italy. This rock is also known as Comiso limestone in two previous publications.[32,33] The Ragusa Formation occurs in monotonic, gently dipping layers of maximum thickness of 60 cm, and is interlayered with unconsolidated clay-bearing strata. Carbonate layers within the formation consist generally of a combination of calcite ($CaCO_3$) and dolomite ($CaMg(CO_3)_2$), or occasionally of pure calcite. At the intralayer scale, the fabric is visually isotropic, and our samples all looked similar in terms of colour and colour variation (Figure S1). This limestone is composed of calcite (~95%–98%), a small amount of quartz (~2%–3% wt) and possible traces of dolomite, as determined from X-ray Diffraction and X-ray Fluorescence.[32]

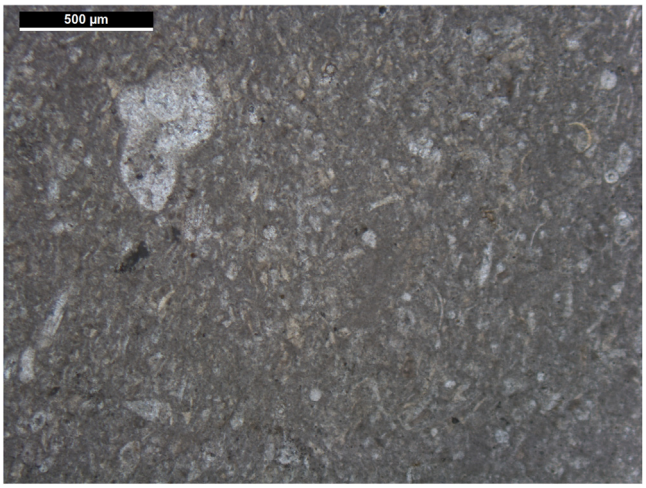

Fig. 1. Optical Microscopy (plane polars) image of sample CL2-4, taken as far from the fracture zone as possible, assumed to be representative for intact material in terms of grain size.

Cylindrical samples of 54 mm diameter were cored using a radial drilling machine tool equipped with diamond tipped hollow barrel. The cylinders were then trimmed with a diamond-tipped rock saw so that the length diameter ratio was approximately 2:1; the end surfaces ground to a flatness of <20 µm using a surface grinding machine tool. Based on the similar look in terms of colour, colour variations and grain size between the samples, only small differences in sample composition were expected. An image of the matrix far away from the damage zone in one of the post-experimental thin sections is shown in Fig. 1 to have a rough indication of what the starting material looks like.

Since limestone rocks often exhibit porosity variations within the same lithology, we have measured porosity of all the samples before testing. The sample's porosities vary between 7.5 and 26.3% (see Table 1), with an average at 14.6%, and an average density of 2.47 g/m^3, determined following a standard saturation and buoyancy technique before long-term exposure (i.e. immediately after vacuum saturation). Throughout the paper, when porosity is mentioned, we refer to this pre-testing sample porosity. The samples from the same blocks used by Castagna et al.[32] have a reported porosity of 10.1%, which falls in the range of porosities covered by the samples used in the current study. Note that Bakker et al.[33] performed high temperature experiments on samples from the same quarry but from a different sampling campaign. Their samples had a lower initial average porosity of 8.7%, and, based on their description, contained more dolomitic material than the samples tested here. We note that a lower porosity and higher dolomite content can lead to strengthening[34,35]; therefore, we do not compare our results to those obtained by Bakker et al.[33]

2.2. Methods

2.2.1. Sample assembly and testing procedure

We placed each sample between two hardened steel platens and then encased in a heat-shrink Polytetrafluoroethylene (PTFE)

Table 1
Experimental parameters and main results. "sat" stands for saturated. Stresses are defined in Section 2.2.2; all are given as ($\sigma 1$–$\sigma 3$). NLM (non-local-means) filter parameters are only given for those samples for which micro-tomography was obtained. Our reference samples are samples in the presence of a saturated $CaCO_3$ solution.

Sample	Effective porosity (%)	Saturated density (Mg/m^3)	Saturation duration (days)	Confining pressure (MPa)	Mechanical behaviour	Crack initiation differential stress (MPa)	Unstable crack growth differential stress (MPa)	Differential maximum (peak) stress (MPa)	C* (MPa)	Ductile differential yield stress (MPa)	NLM-filter parameters
Reference $CaCO_3$ (sat)											
CL3-4 ref	12.83	1.76	1	7	brittle I	28	54	59			20-4-0.75
CL2-6 ref	21.53	2.29	1	7	brittle I	27	54	56			
CL3-1 ref	12.73	2.76	1	30	brittle I	41	116	123			
CL2-5 ref	13.60	2.38	1	70	ductile				49	178	
0.4 M $MgSO_4$ + $CaCO_3$ (sat)											
CL2-4 Mg S	13.55	2.36	1	7	brittle II	55	75	94			30-4-0.7
CL3-3 Mg S	13.54	2.18	1	30	ductile				31	111	25-6-0.9
CL1-8 Mg L	8.85	2.31	50	7	brittle II	143	185	203			
CL1-9 Mg XL	10.02	2.48	200	7	brittle I	107	126	157			20-6-0.75
CL1-4 Mg XL	7.51	2.51	200	30	brittle I	169	212	242			
CL2-7 Mg XL	7.87	2.36	200	70	ductile				24	92	
0.4 M Na_2SO_4 + $CaCO_3$ (sat)											
CL3-8 Na S	14.62	2.18	1	7	brittle I	34	58	61			20-3-0.75
CL3-2 Na S	14.54	2.28	1	30	brittle I	38	116	118			
CL3-7 Na S	14.66	2.28	1	70	ductile				79	177	
CL3-5 Na L	FAILED	FAILED	50	7	brittle I	32	58	62			
CL2-3 Na XL	26.28	2.29	200	7	brittle I	62	81	97			
CL2-8 Na XL	8.14	2.38	200	30	brittle I	42	70	76			20-4-0.75
CL2-2 Na XL	22.78	2.38	200	30	ductile				34	72	20-4-0.75
CL2-1 Na XL	22.25	2.36	200	70	ductile				30	84	

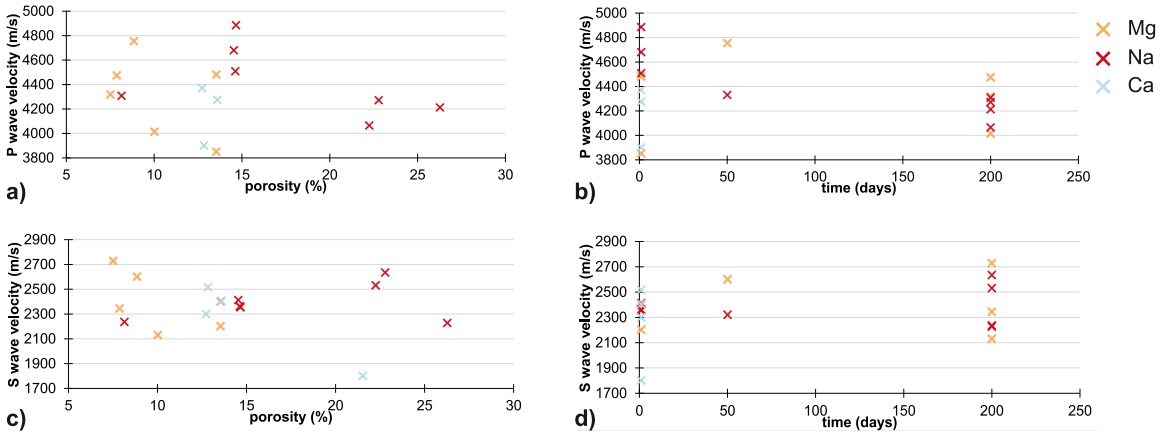

Fig. 2. Wave velocities as a function of porosity and exposure time.

membrane to prevent ingress of confining fluid into the rocks. Three piezo-transducers, one for P-waves and two for S-waves polarized at 90° from each other, were embedded in each platen for measuring ultrasonic velocity in the axial direction of loading. The samples were then instrumented with two axial extensometers (MTS 632.90F-12, accurate to ±0.01%), positioned diametrically opposite each other over the central 50 mm of the sample, and a circumferential chain extensometer (MTS 632.92H-03, accurate to ±0.01%) positioned at mid-length. A third platen, not part of the aforementioned sample assembly, was spherically seated to prevent eccentric loading. This spherically seated platen was in turn fixed to a 2.6 MN capacity force transducer (MTS 661.98B.01, accurate to ±0.32% of load) to measure the vertical load applied to the sample. Finally, empty pore fluid tubing was connected to the top and bottom platens to allow for any pore fluid to flow out of the sample without uncontrolled pore pressure build up during deformation and thus ensured macroscopic drained conditions.

Triaxial testing was undertaken in a (commercially available) MTS 815 servo-controlled stiff frame inside a vessel capable of a confining pressure up to 140 MPa. A schematic of the apparatus is shown in Fig. 3 [for more details, see Ref. 36]. All experiments were performed at room temperature in an environmentally controlled chamber at 20 °C. Once the sample assembly was mounted in the vessel, an initial axial pre-load of 2.3 kN (i.e. 1 MPa; well within the elastic domain of the material) was applied, to ensure a stable contact and alignment of the platens. The confining pressure vessel was then closed and filled with mineral oil confining fluid. Both pore fluid outlets were left open to atmosphere for the drained conditions. Note that Bakker et al.[33] performed drained experiments on lower porosity and stronger Ragusa limestone, and no pore fluid pressure build-up during deformation was reported. A differential stress of about 1 MPa was maintained whilst the confining pressure was increased at 2 MPa/min to the desired confining pressure of 7, 30 and 70 MPa, respectively. Subsequently, axial loading was initiated in constant axial strain rate control of 5.0×10^{-6} s^{-1}, controlled directly from the average of the two axial extensometers. When the sample was approaching peak stress, control was switched to circumferential extensometer control at a corresponding rate of $1x\ 10^{-3}$ mm s^{-1},

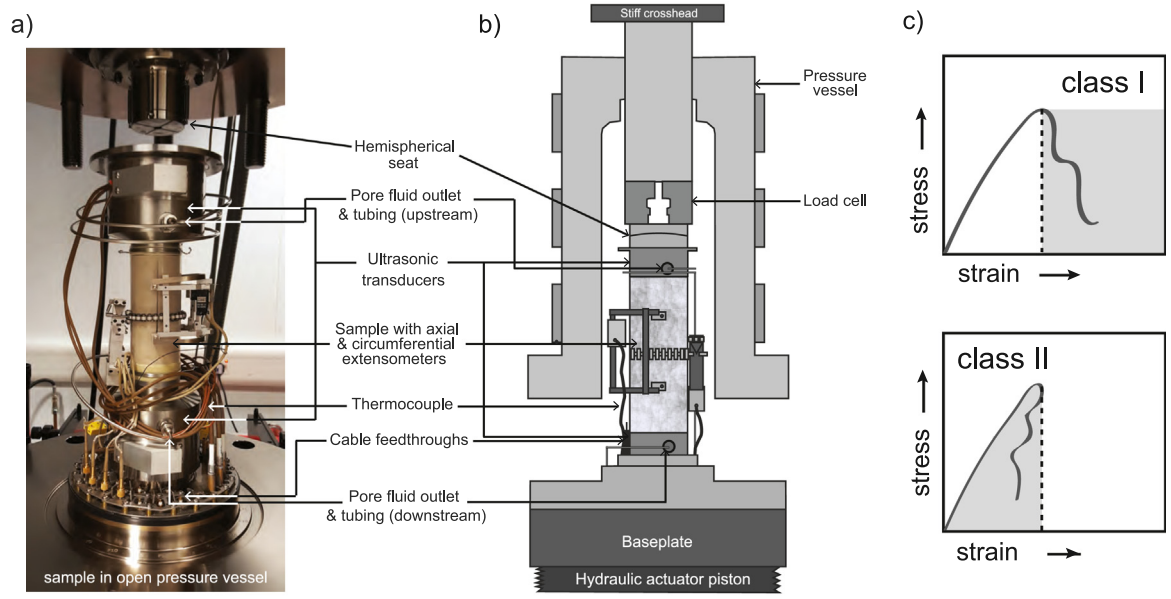

Fig. 3. (a) Photo of the sample assembly in the triaxial apparatus; (b) schematic of the apparatus [see also] Ref. 32; note that the samples are 54 mm in diameter, and c. 120 mm in length. The axial and circumferential strains of the sample are measured directly on the sample; (c) schematic definition of class I vs. class II behaviour.[33]

thus keeping the axial strain rate constant whilst macroscopic failure occurred (Figure S2 for example curves of axial strain rate versus time). Using the lateral displacement feedback signal is a standard control method[37] to capture the full stress–strain characteristics of both Class I and Class II rock failure (Fig. 3c), the two potentially observable failure modes of rocks in stiff rigs.[37–42] Class II is indicated by a negative to vertical slope $\Delta(\sigma 1\text{-}\sigma 3)/\Delta\varepsilon\text{-}_a$[42] (Fig. 3c). The experiment was continued until a residual strength stage was reached or a significant amount of axial strain was recorded (between 2% and 5%). In addition, during each test, 5 ultrasonic velocity measurements were done using the classical ultrasonic pulse transmission technique [e.g.] Refs. 43, 44: (i) at 1 kN of axial loading (open cell), (ii) at 2.3 kN of axial loading (cell filled with oil), (iii) once confining pressure was reached, (iv) at onset of dilatancy (departure from linear elastic behaviour in axial strain), and (v) just before terminating the test (either residual or maximum axial strain recorded). The first two ultrasonic velocity measurements, not reported here, were done for calibration purposes only. The third ultrasonic velocity survey is used to probe the material characteristics prior to axial loading (Fig. 2). The differential stress increase was briefly paused during the fourth ultrasonic velocity measurements to ensure the sample was at steady state during the measurement.

The porosity variation noted earlier indicates some sample heterogeneity is present, and could potentially impede seeing any effect from the sample's exposure to different fluids. One way to address the effect of initial sample heterogeneity and exposure duration on material properties is to compare for all samples how the ultrasonic velocities taken before loading varies (i.e. as soon as the sample has reached target confining pressure; measurement iii in the above description). These velocities are expected to reflect the sample characteristics prior to deformation though increased confining pressure slightly modify the microstructure (closing cracks for instance) and results in higher velocities than at ambient conditions.[45] For all samples here, the P-wave velocity V_p and S-wave velocity V_s are within expectation for carbonate formations,[46] and exhibit a slight decrease with increasing porosity (Fig. 2). Note especially that there is no obvious correlation between velocity (and therefore of initial sample heterogeneity) with pore fluid type or with exposure duration (Fig. 2b, d). This lack of correlations supports our initial assumption that the exposure to our different fluids does not lead to large changes to the grain structure (cementation or dissolution), i.e. we assume chemical reactions changing the sample structure are absent during exposure – as also confirmed by the PHREEQC models.

The axial load, axial load actuator displacement, axial stress (σ_1), differential stress ($\sigma_1 - \sigma_3$), confining pressure P_c ($= \sigma_2 = \sigma_3$), confining pressure actuator displacement, axial strain (ε_{ax}), circumferential strain (ε_{circ}) and temperature were monitored throughout the experiments and recorded at two independent sampling frequencies of 1 s (i.e. sampling frequency based on time) and 500N (i.e. sampling frequency based on force, to ensure recording of multiple data points during rapid stress drops). Furthermore, note that since displacement and force were measured directly on the sample (Fig. 3), no additional corrections are necessary to derive strain and stress from displacement and force data respectively. All experiments are listed in Table 1. A limited number of repeat experiments was undertaken (constrained by sample availability): $CaCO_3$, S treated samples at 7 MPa of confining pressure and XL exposure to Na_2SO_4 at 30 MPa of confining pressure. This allowed us to further assess the importance of sample variability and starting porosity for this specific rock type. Note that the Mg-exposure reproducibility test is not presented as the planned repeat sample was unexpectedly damaged before testing.

2.2.2. Data processing

We determined the static Young's modulus E_{stat} as the slope coefficient of the linear portion of the stress–axial strain curve, chosen as 25 to 75% of peak stress, which ensured a repeatable procedure. We calculated the dynamic Young's moduli using the ultrasonic velocity measurements (V_P, V_S) and saturated densities ρ_{sat} of the samples[47]: $E_{dyn} = \rho_{sat} V_S^2 \frac{3V_P^2 - 4V_S^2}{V_P^2 - V_S^2}$. We note that in material science homogeneous materials, such as pure metals, have equal static and dynamic moduli. In rocks, significant differences between static and dynamic are expected due to their heterogeneities in comparison, where the dynamic parameter is almost always larger than the static one [e.g.] Refs. 48–51.

In the brittle regime, i.e. for the samples exhibiting a maximum stress in the stress–axial strain graphs, followed by mechanical weakening, we determined the key damage points as follows [c.f.] Ref. 52: (i) the crack initiation stress, taken as the stress at which the stress–axial strain curve deviates from linearity; (ii) the stress at which unstable crack growth commences, taken as the maximum in accumulated volumetric strain, and (iii), the peak stress, observed in the stress–axial strain curve as the point of maximum stress. We define macroscopic ductile behaviour by a continuous strain hardening without strength loss, following the classical definition by Rutter.[53] In this ductile regime,[53] we determined the onset of shear-enhanced compaction, observed as the inflection point (deviation from linearity) on the stress-volumetric strain curve (i.e. similar to C* from Wong et al.[54] or Vajdova et al.[55]). Since we lack hydrostatic experiments for comparison we choose to define this parameter in this manner. We also used the maximum volumetric strain for those curves that exhibit a transition from compaction to dilatancy, to represent ductile yield or "failure" in the ductile regime.[54]

2.2.3. Micro-tomography and microstructure

After the experiments, the samples that failed in the brittle regime were scanned with a NanoTom microtomograph at TU Delft, using a resolution of 60 μm/voxel. Samples were scanned in full size, i.e. 54 mm diameter, and 108–125 mm high. Note that fracture aperture needs to be about twice the voxel size to be accurately resolved. Using Avizo© software (version 9) all scans were processed, similarly to Pluymakers et al.[56] Before fracture extraction all samples were filtered with a non-local-means filter, which is an edge-preserving filter.[57] The parameters are listed in Table 1. They are respectively window size, the local neighbourhood and the similarity value, and are related to a combination of fracture aperture and length, matrix grain size and level of denoising necessary. Movies of the slices and extracted fractures are shown in Movie S1–S7. Furthermore, attempts were made to produce thin sections of areas comprising the principal damage zone in the samples. Unfortunately, only two low quality thin sections were eventually done (samples CL3-6 and CL2-4); the other samples' damage zones were lost in the process due to inappropriate methodology. The micrographs presented here were obtained with a standard optical microscope outfitted with a camera, and backscatter electron images were obtained using a scanning electron microscope.

3. Results

3.1. Mechanical results

We focus here only on the impact of the ion species and address the concomitant role of the porosity in a dedicated section of the discussion.

Detailed results of sample loading and failure behaviours are shown in Fig. 4. At 7 MPa, the shape of the resulting stress–strain curves show differences between the ion species (Fig. 4a; b). All samples exhibit brittle failure, i.e. peak stress followed by strength loss. However, only those samples exposed short (1 or 50 days) to $MgSO_4$ exhibit class II type failure, indicated by the negative to vertical slope $\Delta(\sigma 1\text{-}\sigma 3)/\Delta\varepsilon_a$ and high dilatancy post-failure. For the reference solution, the samples behaved brittle at 30 MPa, and ductile at 70 MPa – i.e. following the trend as reported by Ref. 32 for dry and wet Ragusa limestone. In the presence of $MgSO_4$ the short exposed sample at 30 MPa already behaved in a ductile manner, and the 200 days exposed sample still behaved brittle, which can point to an early onset of the brittle–ductile transition compared to the dry, wet and $CaCO_3$ saturated samples[32 and this study, respectively]. In the presence of Na_2SO_4, two of the three samples tested at 30 MPa, one S and one XL, behaved ductile. The repeat samples exposed to $NaSO_4$ for 200 days (XL) failed in a brittle manner, i.e. a similarly early onset of the brittle–ductile transition as for $MgSO_4$. All samples tested at 70 MPa exhibited ductile behaviour.

Comparing the key stresses as defined in Section 2.2.2, there are clear differences in the geomechanical behaviour of the samples as a function of the ion species exposure (Fig. 5), both in the brittle field and the ductile field. Fig. 5a includes also the peak stresses of dry and wet Ragusa (Comiso) limestone from Ref. 32 for comparison. Comparing our reference samples with $CaCO_3$-saturated solution to those tested with 24 h exposure to deionized water[32] (i.e. experiments in which the pore fluid is undersaturated with respect to $CaCO_3$, similar to[17]), $CaCO_3$-saturated solutions lead to weaker samples than those in undersaturated water. They are at 7 MPa only half as strong, and at 30 MPa only 4 MPa weaker (Fig. 5a). We performed a repeat experiment at 7 MPa for two samples with a porosity of 12.8 and 21.5% respectively, which indicated all three key stresses varied within 5 MPa. Comparing the key stresses within our own reference dataset, the stress difference at which unstable crack growth commences and the peak stress in the brittle field lie very close, only 5 to 10 MPa. The key stresses for samples tested both at 7 and 30 MPa (regardless of S, L or XL exposure) all line up, with the ones for the sample tested at 30 MPa exhibiting slightly larger difference (Fig. 5b). The slope between the three key stresses is shallower at 30 MPa than at 7 MPa. The ductile yield stress (the stress at which dilatancy takes place) in the 70 MPa test is at a higher stress than the peak stress of the brittle samples (Fig. 5d).

All $MgSO_4$-exposed samples that behaved brittle are shown in Fig. 5b. For 24 h exposure to $MgSO_4$, at 7 MPa it was 13 MPa stronger than the reference sample. With prolonged exposure all key stresses increase, and the peak stresses for the samples (all low porosity samples, similar to those from Castagna et al.) with 50 and 200 day exposure time are the highest in the dataset: 40 (at 7 MPa) and 60 MPa (at 30 MPa) higher than for the dry samples. Given that dry strength was 116 and 160 MPa respectively,[32] this represents a ~35% strength increase due to $MgSO_4$-exposure. In the brittle field, at comparable confining pressures $MgSO_4$ leads to an increase of >20 MPa in all key stresses compared to the reference dataset. For each individual sample, the difference between the key stresses is about 20 to 30 MPa. The slope between the key stresses and confining pressure is the same, regardless of confining pressure applied and exposure duration. Ductile yield in the presence of $MgSO_4$ occurs at lower stresses than the brittle peak stresses (Fig. 5e) (i.e. different from what is observed for the reference dataset).

For 24 h exposure, in the brittle regime, the Na_2SO_4 samples exhibit similar behaviour to the reference dataset, both in terms of stress magnitude as relative position of the different key stresses to one another (compare Fig. 5a to c). However, at 50 and 200 days exposure time, confining pressure becomes important: where at 7 MPa Na_2SO_4 values are the same to the reference, at 30 MPa Na_2SO_4 key stresses are below those of the reference strength (regardless of starting porosity). With 76 MPa, peak stress at 30 MPa is only about half that of dry rock from Castagna et al.[32] The repeat experiment with XL exposure and porosity on both ends of the spectrum indicated brittle behaviour for the low porosity sample (CL2-8; 8.14% porosity) and ductile behaviour for the high porosity sample (CL22-3; 26.27% porosity). They do exhibit the same brittle peak stress as the ductile yield stress. The ductile yield stresses at 70 MPa fall below those of the reference dataset and those exhibited by $MgSO_4$ samples (Fig. 5f). Overall, the key stresses for the Na_2SO_4 samples do not exhibit a strong dependence on confining pressure. In both the brittle and in the ductile regime the samples with 200 day Na_2SO_4 exposure are the weakest in the dataset.

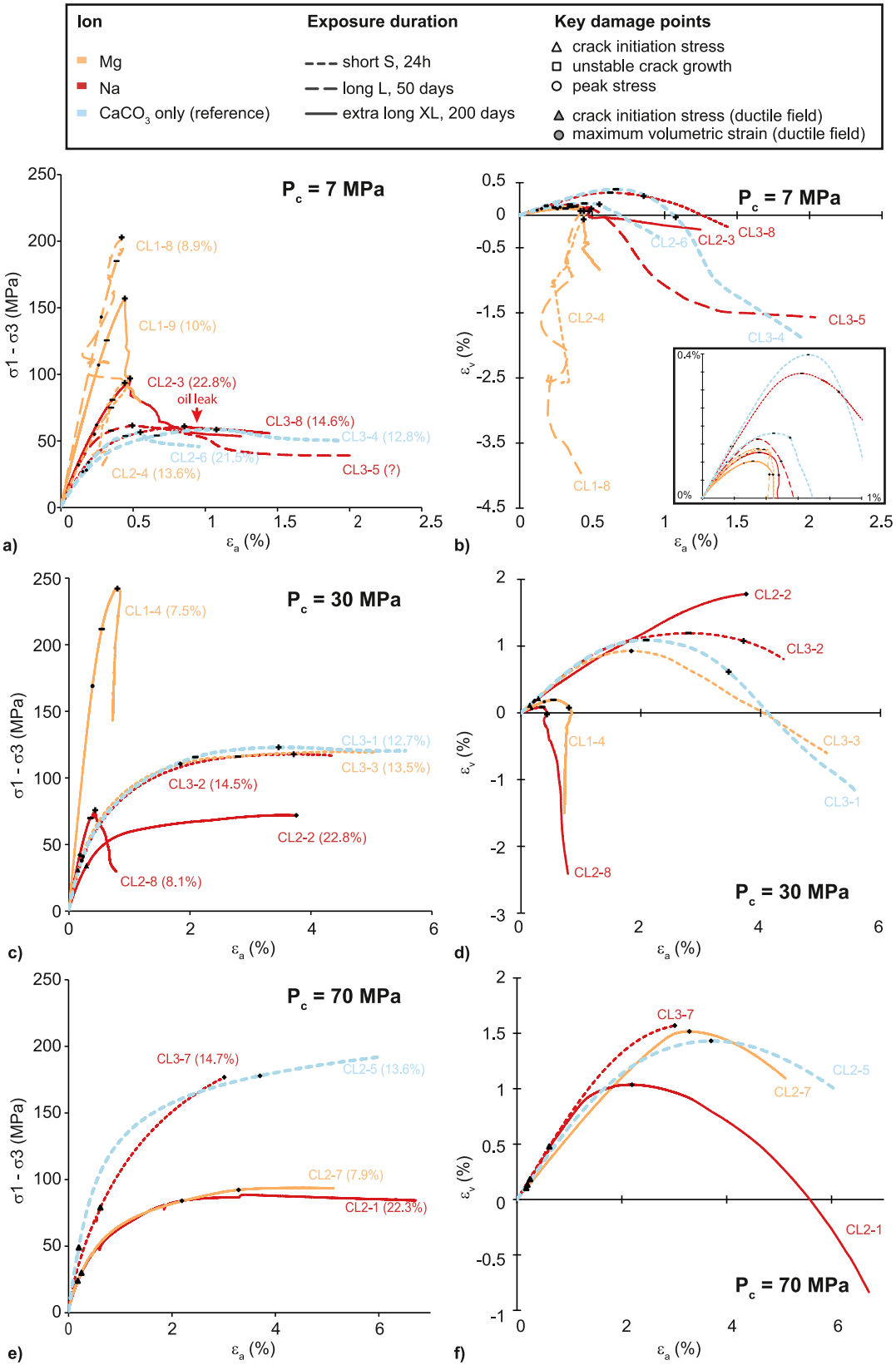

Fig. 4. Stress–strain curves for all experiments, with axial strain ε_a vs. stress $(\sigma_1 - \sigma_3)$ on the left side, and axial strain ε_a vs. volumetric strain ε_v on the right side. The short dips in the loading curve in the stress–strain plots are related to a brief halt of the drive motor to perform acoustic velocity measurements. Legend on top of the figure – Mg stands for exposure to 0.4 M $MgSO_4$ (+$CaCO_3$ (sat)) solution; Na for exposure to 0.4 M Na_2SO_4 (+$CaCO_3$ (sat)) solution. Key damage points as defined in Section 2.2.2are indicated with corresponding markers; (a–b) for P_c = confining pressure 7 MPa; (c–d) 30 MPa; (e–f) 70 MPa.

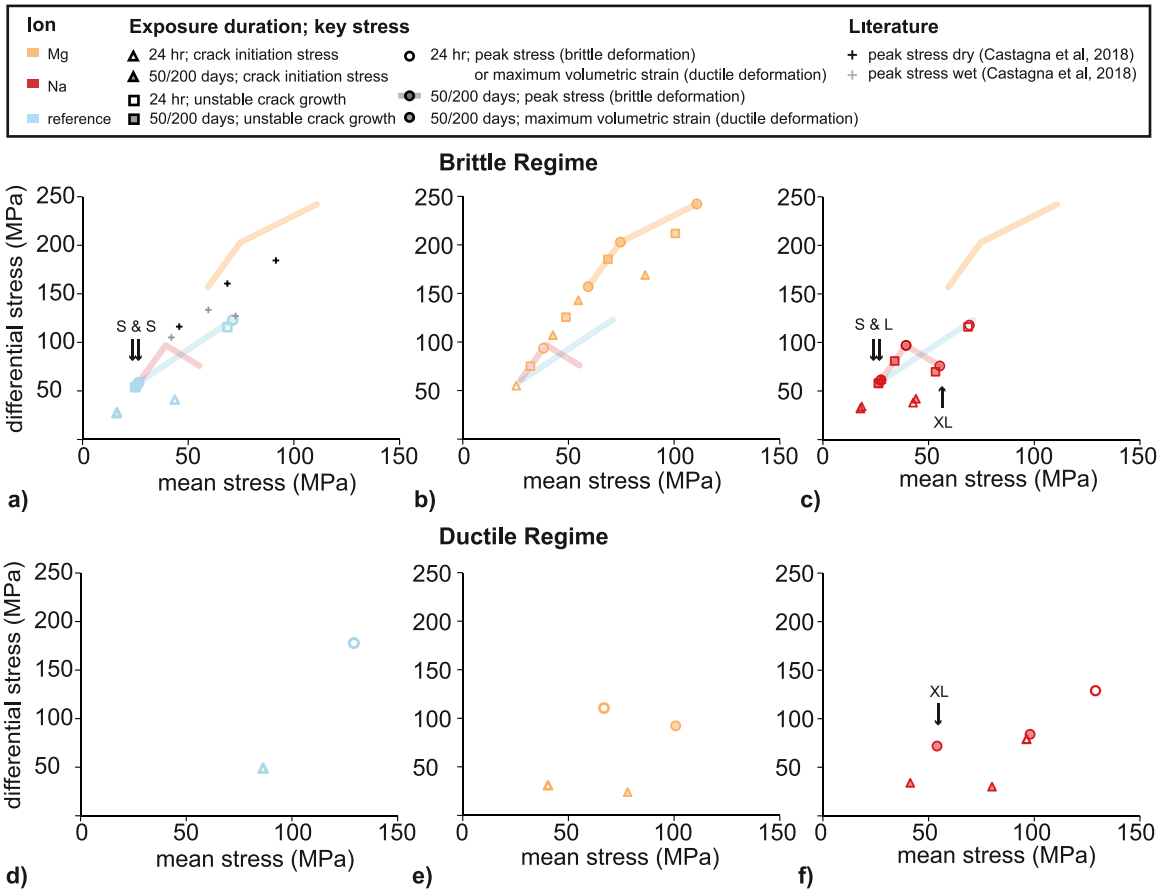

Fig. 5. Summary of key stresses, legend on top – Mg stands for exposure to 0.4 M $MgSO_4$ (+$CaCO_3$ (sat)) solution; Na for exposure to 0.4 M Na_2SO_4 (+$CaCO_3$ (sat)) solution. To guide the eye, in the brittle field (a–c) the connection between peak stresses for the reference samples and for the 50/200 days exposure to $MgSO_4$ and Na_2SO_4 is indicated with semi-transparent lines. Repeat experiments indicated with arrows, where S stands for 24 h exposure, L for 50 days exposure, and XL for 200 days exposure; (a) reference data, obtained with $CaCO_3$ saturated solution, for the brittle field. This plot also contains the dry and wet peak stresses from Castagna et al.[28]; (b) $MgSO_4$ data; (c) Na_2SO_4 data; (d) reference data for the ductile field; (e) $MgSO_4$ data; (f) Na_2SO_4 data. Note that the experimental error is significantly smaller than the symbol size.

3.2. Static and dynamic Young's moduli

Fig. 6 summarizes the ultrasonic velocity measurements done along with the calculated dynamic and static Young's moduli for each test. As expected, for most experiments, the velocities increase going from the measurement before loading (point 1) to the measurement before failure (point 3), and then decrease at post-failure point 4. This is consistent with the interpretation that between points 1 and 3, microcracks close, followed by linear elastic deformation until unstable crack growth commences (Figs. 4, 5 and side schematic in Fig. 6). This volume modification reduces the elastic wave interaction with the travelled medium, hence leads to increased velocity values. Subsequently, at point 4, the samples have either failed in the brittle regime or were strengthening with displacement in the ductile regime. Either way, a network of microcracks is assumed to have been induced and either led to macroscopic sample failure along the shear plane (brittle regime), or to the expected grain comminution associated with strengthening (ductile regime). As confining pressure increases, the velocity changes within a single sample are smaller, and the overall spread of the velocity measurements taken at one point is narrowing, which likely reflects better contact between sample and transducers. Differences between the static and dynamic Young's moduli can also be noticed, with dynamic ones being almost always larger than static ones as expected.[48–51] There is one additional pattern visible, which correlates to ion exposure: at 7 MPa, only the $MgSO_4$ exposed samples have overall higher static than dynamic Young's moduli (Fig. 6). These differences found in experiments between static and dynamic moduli are usually interpreted to be related to local drainage conditions when the measurements were taken and/or as a result of non-elastic processes during monotonous loading over a finite range [e.g.] Ref. 51. Note there is no specific relation between the ultrasonic velocity measurements and failure class (class I; CL1-9 – XL vs. class II; CL1-8 L and CL2-4 S), nor is there a correlation with sample porosity. These ultrasonic velocity measurements independently confirm that $MgSO_4$ exposure has a measurable impact on the sample at low stress conditions, with a different signature from that of exposure to $CaCO_3$-only or Na_2SO_4 exposure.

3.3. Microtomography scans

We first qualify the post-mortem sample scale induced damage using 3D reconstructed volumes from micro-tomography scans. Fig. 7 and Movies S1–S4 show the damage within the samples deformed at 7 MPa of confining pressure; Movies S5 and S6 are for the samples deformed at 30 MPa and that failed with large stress drops. Movie S7 show the damage within sample CL2-2 (Na_2SO_4 exposure for 200 days) deformed at Pc = 30 MPa that exhibited ductile behaviour. Due to the resolution limit of the scanner of 60 μm per voxel, only the samples with macroscopic damage were scanned (since damage visible to the eye means it is also visible damage in the scanner).

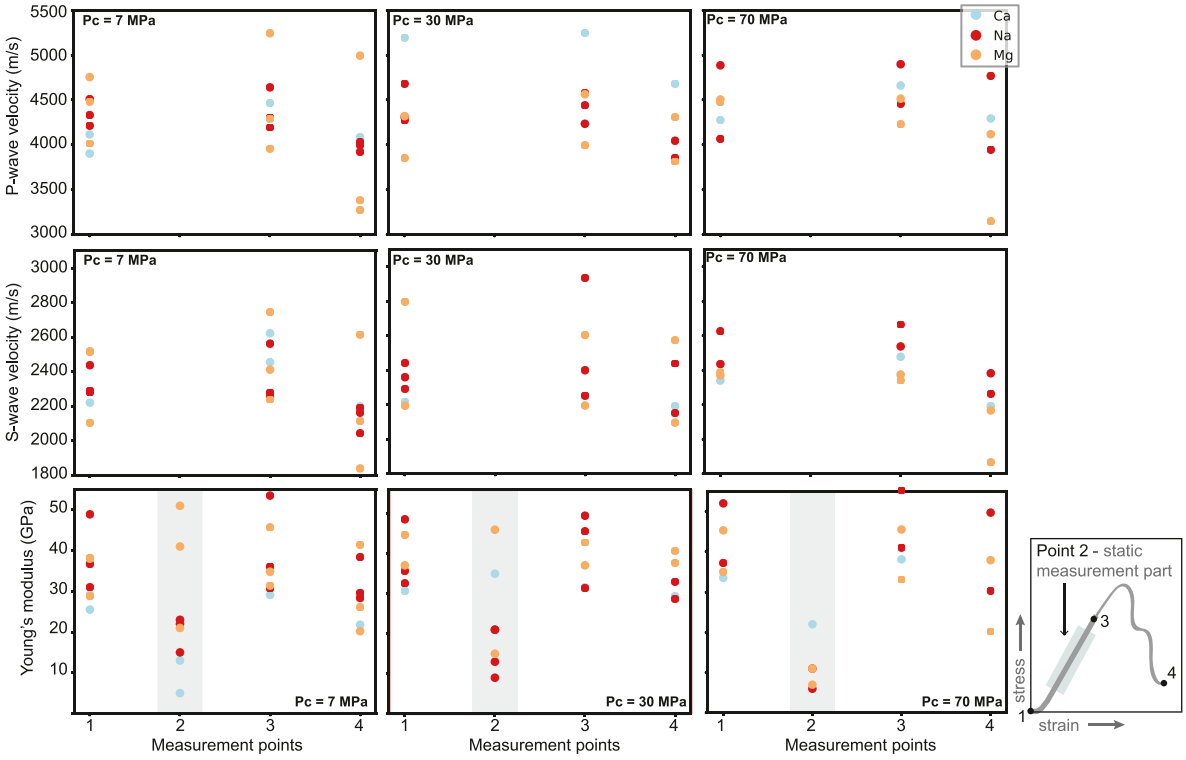

Fig. 6. Summary of ultrasonic velocity measurements (Vp in top row plots, Vs in mid row plots) and calculated Young's moduli (bottom row plots). Grey bands delineate the static moduli plotted along the dynamic moduli, with respective points of measurements during testing as indicated in bottom right corner schematic.

At 7 MPa, the reference sample exhibits a fracture network, i.e. distributed deformation (Fig. 7a; Movie S1). In contrast, for the samples exposed to $MgSO_4$, the micro-tomography scans reveal strongly localized deformation, where CL2-4 (24 h exposure) exhibits a highly localized shear plane in the form of a single fracture with a narrow (a few voxels wide) to not visible damage zone (Fig. 7b and Movie S2). This is also the sample that exhibited the rapid class II failure. The 200 days exposed $MgSO_4$ sample (CL1-9, Fig. 7c and Movie S3) shows a standard conjugate fracture set. The Na_2SO_4 sample (CL3-8, 24 h exposure) exhibits distributed deformation similar to the reference sample (Fig. 7d; Movie S4). At 30 MPa confining pressure the samples that behaved brittle exhibit both a fracture network, i.e. distributed deformation (Movies S5–S6; $MgSO_4$ and Na_2SO_4 respectively). For comparison, the Na_2SO_4 sample that behaved ductile at 30 MPa (Movie S7, CL2-2) only exhibits few internal fractures, none of which crossing through the entire sample width. The microstructural difference in ion species is in line with the observed differences in brittle strength.

Going into greater microscopic details, the optical micrograph for CL2-4 (short exposure to $MgSO_4$; class II; single localized fracture) shows a ~200 μm wide zone of grain size reduction next to the central fracture zone (Fig. 7e). The optical micrograph of CL3-6 (short exposure to Na_2SO_4; class I; distributed deformation) shows multiple fractures infiltrated by epoxy, with a narrow (<100 μm) zone of grain size reduction near where the sample has split (Fig. 7f). The backscatter electron images further indicate that for both samples the grains near the fracture zones contain many intragranular cracks (Fig. 7g–h).

4. Discussion

This being a carbonate, there is unquestionably sample heterogeneity. This is reflected in initial sample colour (Figure S1), sample wave velocity (Fig. 2), saturated density (Figure S3) and porosity (Section 4.1). However, the only consistent correlation is that Mg-exposed samples are stronger than all other samples. There is no systematic correlation between Mg-exposure and any of the other parameters related to sample heterogeneity. Since porosity does exert a major control on strength, in the following, we discuss the potential effect of porosity, followed by potential explanations for correlations between strength and the different pore fluid chemistries.

4.1. Effect of porosity

Previous research on carbonate rocks has indicated that with an increase in porosity such rock becomes weaker [e.g. Refs. 58–61]. Most models based on Hertzian cracking of limestones (with cracks starting at pores) indicate that unconfined compressive strength is controlled by porosity and pore size.[58–60] The pore collapse pressure P* is controlled by the porosity, the size of micropores and the partitioning between micro- and macro-porosity.[58–60] Due to the different initial porosities of our samples, we need an estimate of the maximum effect porosity can have on limestone strength, in order to determine if the effect of pore fluid type is significant in these samples of variable porosity. To obtain a quantitative estimate of the effect of porosity on strength, we plot the data on UCS and on P* as a function of porosity plus the extrapolations obtained by Baud et al.[58] on allochemical Leita limestone in Fig. 8. The underlying assumption is that allochemical limestones share microstructural characteristics which control strength variability. Comparing the available models for the effect of porosity on strength in allochemical limestones,[58–60] it is the extrapolation for P* from Baud et al.[58] that provides the steepest slope of all available strength – porosity relationships. This, to our best knowledge, represents the most extreme effect of porosity on strength available for limestones, and thereby can provide us with a maximum "error bar".

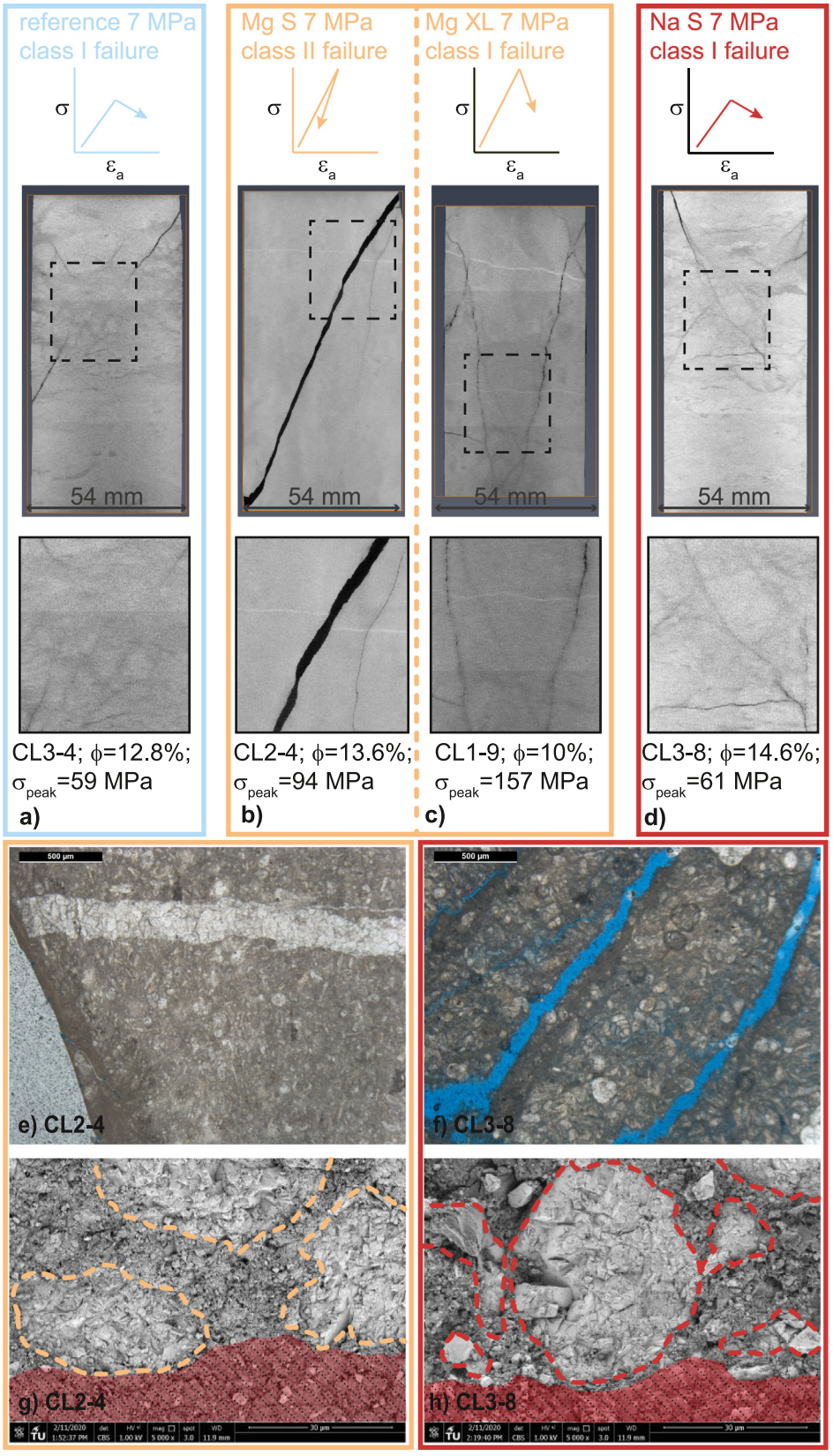

Fig. 7. Summary of sample structure, obtained with x-ray micro-tomography (60 µm/voxel) (a–d) and associated failure behaviour. Complete sample scans are shown in Supplementary Movies S1–S7. From top to bottom, each panel shows the schematic stress–strain behaviour, the full size scan, and a zoom of the main fractured area with the size as the box on the full size scan; (a) the reference case CL3-4, 24 h exposure to saturated $CaCO_3$ solution at 7 MPa, which exhibits the same features as Na_2SO_4 exposure; (b) CL2-4, 24 h exposure to $MgSO_4$, which failed in class II mode and exhibits strongly localized failure; (c) CL1-9, 200 days exposure to $MgSO_4$ (brittle failure in class I mode), with conjugate fractures; (d) CL3-6, 24 h exposure to Na_2SO_4 (brittle failure in class I mode), with a distributed fracture network; (e–f) transmitted light optical micrograph of the central fault zone of (e) CL2-4; and CL3-6; (g–h) electron microscope backscatter image of the edge of the central fault zone, with red, hatched fault zone and outlined grains, of (g) CL2-4 and (h) CL3-6).

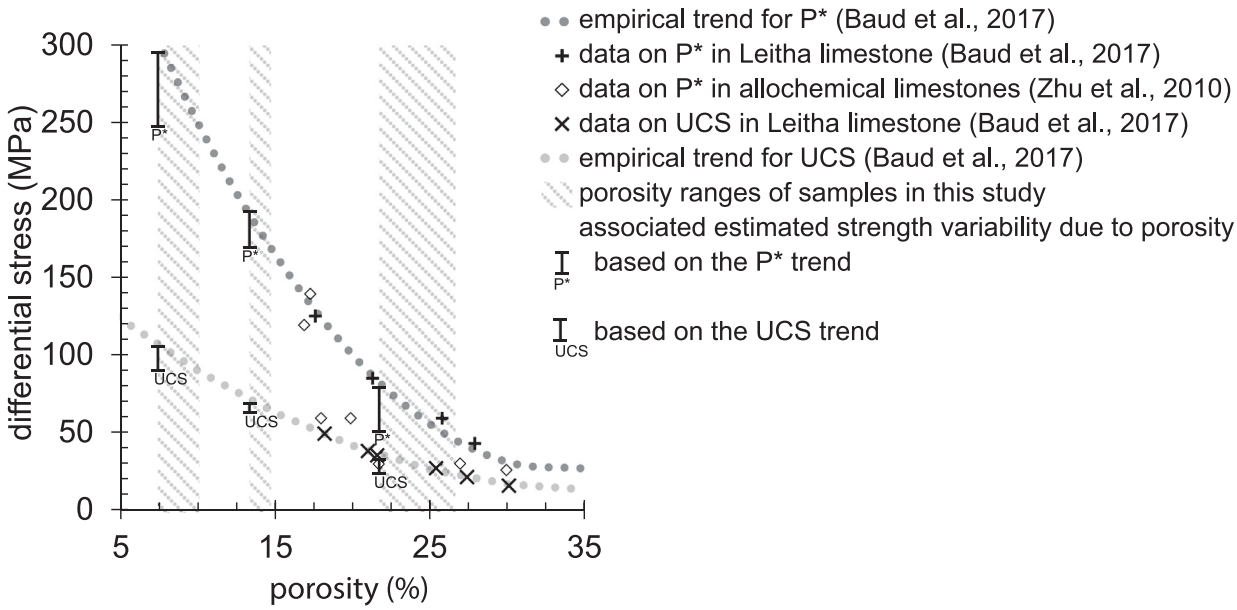

Fig. 8. Data and extrapolated trends for UCS and P*, obtained with Leitha limestone,[58] plus the porosity ranges for the samples used in this study separated in a low, medium and high porosity batch. The intersection between the dashed areas and the P* extrapolation provides an estimate for the potential strength variability that can attributed to porosity differences in this study. This figure is adapted from Baud et al.,[58] and includes data from Zhu et al.[59] for P* obtained on other allochemical limestones.

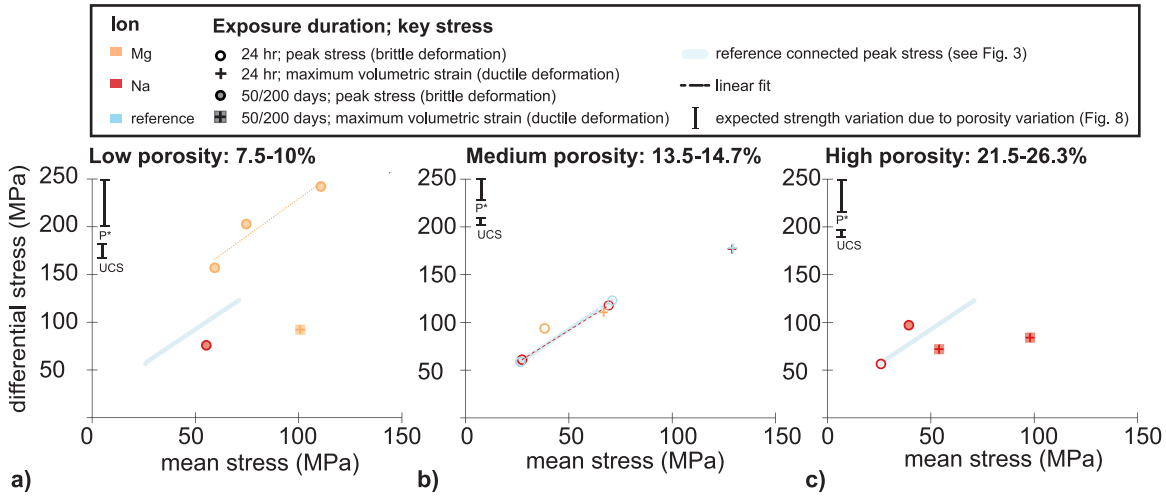

Fig. 9. Peak stress (brittle field) and yield stress (ductile field) versus mean stress as a function of the porosity ranges. Each panel includes the estimate for the maximum strength variations based on the data and models of Baud et al.[58] For comparison purposes, we also include the line of the reference dataset (all medium porosity) in light blue; (a) low porosity samples (7.5%–10%); (b) medium porosity samples (13.5–14.7%); high porosity samples (21.5–26.3%). Open symbols are for S exposure, closed symbols for L/XL exposure.

We then separate the peak stress (brittle field) and yield (ductile field) versus mean stress plot of Fig. 5 in three narrow porosity ranges: low porosity (7.5%–10%), medium porosity (13.5–14.7%) and high porosity (21.5–26.3%), in Fig. 9. Many rock mechanics experiments compare results for samples with a porosity varying around 2%, i.e. this can then be considered a sufficiently small sample batch to allow comparison. Furthermore, by comparing the strength differences in the models from Baud et al. in these porosity regions (intersection of the dashed area with the extrapolation of P* in Fig. 8) we obtain values for an estimated strength variation of 50, 19 and 37 MPa for low, medium and high porosity respectively. Note that if we would use the model for UCS strength, this would be only 16, 6 and 13 MPa respectively. Both estimates of possible strength variations are given on the plot of Fig. 9. In the following, we discuss brittle and ductile failure separately. First, we consider brittle failure. To guide the eye, we have used a simple linear regression analysis to connect the three (Mg, XL exposure, low porosity; Fig. 9a) or two similar data points (Mg, short exposure, and reference samples, medium porosity; Fig. 9b), as an approximation for a failure criterion. Even though this type of interpolation is not statistically robust, it helps to interpolate the results and to quantify the strength differences for a similar mean stress. This clearly shows that XL exposure to $MgSO_4$ leads to an ~80 MPa strengthening compared to XL Na_2SO_4 exposure (low porosity, Fig. 9a). For the medium porosity, short exposure to Mg leads to a slightly higher strength (~20 MPa), compared to the reference and Na-exposed samples (Fig. 9b). This is only just outside the 19 MPa variability that can be explained by porosity (Fig. 8), but it is also the sample which failed with class II failure behaviour. This implies there may be a significant effect of Mg-exposure also at short exposure times. Only two of the high porosity samples

failed in a brittle manner, and all those tested with high porosity were exposed to Na_2SO_4. Considering the ductile behaviour, direct comparison of samples within one porosity category is only possible for the medium porosity samples. Short exposure to Mg led to ductile behaviour already at 30 MPa, and the sample is accordingly weaker than the reference or Na-exposed sample. The XL-exposed samples which failed in a ductile manner all exhibit similar yield stresses, despite the large differences in porosity (compare Mg in panel 9a, vs. Na in panel 9c). In future studies on the effect of pore fluid species and limestone failure, we advise to investigate the brittle and ductile failure regime separately, or to obtain more results in the ductile regime.

To summarize, our results indicate that the effect of pore fluid type on the failure stress can be significant, and exposure duration and deformation regime exhibit a much larger effect than can be explained by existing initial porosity alone. Ion species affects rock strength in the brittle and in the ductile field, especially with prolonged exposure time (∼hundreds of days). There are significant strength changes in the presence of different ion species: Mg-exposure leads to strengthening compared to Na-exposure. The combination of porosity and confining pressure effects makes it difficult to determine the exact magnitude, but qualitatively, all our observations hold even when considering the potential effect of porosity.

4.2. Effect of pore fluid chemistry

4.2.1. Effect of $CaCO_3$ saturation

The ultrasonic velocities for our $CaCO_3$ saturated samples are in agreement with the range of values by Nicolas et al.[18] obtained for water-saturated limestone at similar confining pressures. However, in terms of strength, comparing our reference samples with $CaCO_3$-saturated solution to those tested with 24 h exposure to deionized water,[32] at 7 MPa confining pressure our samples are ∼50 MPa weaker. There is no effect at higher confining pressure or on the brittle/ductile transition. Taking the extrapolations from Baud et al.,[58] at from 10%[32] to 12% porosity (our data) could explain 36 MPa but not the ∼50 MPa difference we found. The strong reduction of strength in the brittle field is intriguing, since previous research has shown a more $CaCO_3$ saturated solution leads to stronger samples, at least at high confining pressure and elevated temperature[17] – though these authors did not test fully saturated solutions. Dissolution in carbonate rocks is shown to lead to decreased elastic parameters and is thus expected to lead to reduced strength.[62] Since our experiments in the presence of $CaCO_3$ saturated solution are weaker than the samples in partially saturated solution, suggesting as well that dissolution should not have played any role. Both sample sets used by Castagna and by ourselves, come from the same blocks. Microtomography showed for our samples on voxel resolution little difference in internal variations in grey scale within each sample, (assumed to reflect the mineral content and/or porosity) in the matrix (Movies S1–S7; Figure S4), and visually, samples were similar. Hence, it seems unlikely this difference is simply an effect of sample variability. Excluding then sample variability as a cause, with the current results, we can only provide a hypothesis for this strong weakening at low confining pressure. Previous researchers have brought forward that water weakening in limestones is related to a reduction of fracture surface energy and K_{IC} in the presence of water.[61] That surface energy plays a role is also indicated by recent nano-scale studies into the reactivity of the fluid film along a freshly cleaved calcite surface indicate that nano-scale friction and surface forces are strongly influenced by fluid composition.[63–66] In this type of atomic force microscopy experiments, fully saturated $CaCO_3$ solutions lead to strong repulsive surface forces between two calcite surfaces.[66] When $CaCO_3$ solution is mixed with inert glycol, it leads to reduced repulsive forces, and depending on the glycol/solution ratio even to adhesion between surfaces. Obviously, it is not possible to make a one-to-one comparison between these nano-scale experiments and between glycol/solution ratio and saturation index, but this does suggest there could potentially be a difference in surface interactions between a partially saturated fluid and a fully saturated fluid, which provides the only potential explanation we are aware off.

4.2.2. Effect of $MgSO_4$ in the brittle field

The only two samples that failed in class II mode were samples in contact with $MgSO_4$. Given that all experiments are performed on the same stiff machine, the occurrence of class I vs. class II in this dataset is unlikely to be a machine artefact (i.e. related to the stiffness of the piston), and instead should be related to the sample plus fluid. Furthermore, class II failure coincided with strong localization, consistent with He et al.,[41] who studied class II behaviour in different rock materials. It is difficult to assess the importance of this difference in dynamic behaviour but its occurrence in Mg-exposed samples and not in Na-exposed samples of similar porosity (CL2-4 vs. CL3-8) is noteworthy. Moreover, the ultrasonic velocities indicate that at low confining pressure, the samples with $MgSO_4$ pore fluid exhibited on average the highest post-failure velocities, which correlates to the smallest amount of damage. This is consistent with the increase in key stresses and the increased difference between these key stresses, i.e. between the crack initiation stress, the stress at which unstable crack growth commences and the peak stress. Combined, this suggests an increase in cohesion in the brittle field – visible in the 24 h exposed sample, and even more pronounced in the 50 and 200 day sample. Moreover, all samples in contact with $MgSO_4$ are stronger than those in the reference dataset, and those in contact for 50 and 200 days, are up to 35% stronger than even dry samples. In the following, we discuss potential explanations for progressive alteration with exposure time to MgSO4: either a mineral-to-mineral chemical reaction or a progressive change in surface processes and/or forces.

Considering chemical reactions, since the solutions are saturated with respect to calcite, no dissolution can take place, as confirmed by a PHREEQC batch reaction model. With Mg-ions and calcite, if a reaction would take place, potential reaction products would be Mg-rich calcite and dolomite. A full conversion to dolomite would lead to significant strengthening [e.g.] Refs. 34, 35. However, dolomite precipitation is slow even at elevated pressures and temperatures. At 60 °C, it takes between 3 and 7 years for minerals to fully form in a reaction experiment.[67] Hence, under the ambient conditions and within the timescale of these baths, there cannot be a complete chemical reaction to either Mg-calcite or dolomite. If experiments would be performed at the right temperature for Mg to enter into the calcite structure, the presence of Mg reduces the thermodynamic stability and thus solubility.[68] At elevated temperatures, flushing through Mg-rich solutions has been shown to decrease the mechanical strength of chalk, interpreted to be related to incomplete formation of Mg-calcite because of the high number of defects.[69,70] Given that we observe strengthening instead of weakening an incomplete reaction to Mg-rich calcite of dolomite is not possible.

Since chemical reaction between $MgSO_4$ and calcite is ruled out, a potential hypothesis for our results would be a progressive change in surface processes/forces, related to ongoing diffusion and distribution of Mg-ions into the electrical double layer throughout these porous rocks. The Mg-ion is a dissolution and precipitation inhibitor for carbonates.[71] If grain-scale dissolution/precipitation plays a role in controlling limestone failure, this inhibiting effect may explain why limestones are stronger in

the presence of $MgSO_4$. Moreover, the Mg-ion also leads to an increase in zeta-potential of the surface layer.[28] It is attached to the Ca-ion through a OH-bridge. This positive charge could lead to increased bond strength, thus explaining the increase in yield and peak strength with Mg-exposure. Along similar lines,[64] postulate that the presence of fully hydrated magnesium ions could lead to a significant increase in nano-scale friction, where fully hydrated Mg-ions can penetrate the hydration layer at the surface and form a more rigid hydration shell. A new hypothesis that follows from the here presented work is that it is not water activity,[19] but zeta potential that controls failure of soluble rocks, i.e. those prone to fluid–rock interactions. We cannot distinguish between these effects with the current results.

4.2.3. Effect of Na_2SO_4 in the brittle field

In comparison to the results obtained with $MgSO_4$, samples in contact with Na_2SO_4 samples are on average relatively weak (Figs. 5 and 9), particularly against the Mg-exposed sample of similar porosity (Fig. 9a). Compared to the reference dataset, the results are more ambiguous, as relatively few samples of similar porosity have been tested. However, combined with the apparent insensitivity to confining pressure (Figs. 5 and 9) and the distributed deformation (Fig. 7), it may suggest an early onset of the brittle–ductile regime. Note that weakening in the presence of Na_2SO_4 was also suggested by Bergsaker et al.[26] for the propagation of cracks through calcite crystals. It has also been shown in mechanical tests of chalk, where weakening by Na_2SO_4 flooding was attributed to SO_4 adsorption to the CO_3-ions of the calcite lattice. For an ionic strength of 0.1 the presence of Na_2SO_4 leads to a negative zeta potential.[28] The accompanying repulsive surface charge was postulated before to drive the granular contacts apart.[23,24] However, given that the Mg-experiments contained an equal amount of sulphate and led to strengthening instead, it indicates that this effect of sulphate is not the whole story: there is an effect of the cation that determines the final effect on failure dynamics and limestone strength.

4.2.4. From nano-scale to sample scale

On the nano-scale, Atomic Force Microscopy and Surface Force Apparatus experiments have determined the effect of ions on surface forces and friction of nano-surfaces,[63–66] which is postulated to have implications for deformation of carbonate rocks. These nano-scale results (mostly obtained under room conditions) indicate nano-scale surface forces are affected by the properties of the hydration layer in the grain boundary fluid film, and as such are expected to be significantly affected by ion content. For example, increased concentrations of NaCl lead to increased adhesion between freshly cleaved calcite surfaces[65] and decreased friction between sliding calcite surfaces, and $CaCl_2$ solutions promote frictional weakening even more than NaCl.[64] Experiments on the nano-scale use equilibration times on the order of tens of minutes[64,65,72] up to hours.[63] Going up from the nano-scale, this work was inspired by the significant effect of ion species on crack propagation in cm-sized calcite single crystals.[26] The experiments presented here indicate that the effect of ion species on failure of cm-scale limestone samples is also significant, highlighting more research is needed at all sample scales and with various experimental approaches to fully understand fluid–rock interactions.

5. Conclusions

We set out to determine the effect of $MgSO_4$ and Na_2SO_4 solutions, saturated with $CaCO_3$, on the strength of Ragusa limestone (in literature also referred to as Comiso limestone). We have followed a standard rock mechanics approach, and tested visually similar samples using these different pore fluids, as well as reference data samples with $CaCO_3$-saturated solution only. We also compare our samples to literature data on strength of dry and wet Ragusa limestone, obtained from the same blocks.[32]

In the brittle field, we found that a one-day exposure to $MgSO_4$ led to strengthening compared to the reference solution, whereas a 50 and 200 days exposure led to the strongest samples in the dataset, and up to 35% stronger than even dry rock. A one-day exposure to Na_2SO_4 did not affect sample strength, but a 50 to 200 days exposure led to the weakest samples in the dataset, with about half the strength of dry Ragusa limestone. In the ductile field, both $MgSO_4$ and Na_2SO_4 led to ductile behaviour also at 30 MPa confining pressure, whereas dry and wet Ragusa limestone undergoes the brittle/ductile transition at 50 MPa confining pressure. Samples exposed to $MgSO_4$ were more strongly localized than those exposed to Na_2SO_4, and the 24 h and 50 days exposed $MgSO_4$ samples exhibited class II failure. Moreover, at 7 MPa, the $MgSO_4$ exposed samples have higher post-failure wave velocities (both V_p and V_s) and dynamic Young's moduli than the other samples. This shows that the effect of ion species is present in all key stresses describing rock failure, as well as being accompanied by changes in failure dynamics and associated geophysical and microstructural changes. Since our samples exhibited a range in porosities, we also consider the effect porosity can have on rock strength. Comparing only the results of samples within an initial 2% porosity range indicates significant strengthening after Mg-exposure. This strengthening of Mg-exposed samples, coinciding with microstructural changes and differences in stress–strain behaviour cannot be correlated to differences in initial sample looks, initial sample density, initial wave velocity or porosity. The conclusion of strengthening with $MgSO_4$ versus Na_2SO_4 exposure is robust. The simple cation change in the same salt tremendously affects rock strength and failure dynamics. Comparison to geochemical literature and a batch reaction model indicated that conditions of the bathing time and experiment (ambient conditions and duration) are unsuitable to allow for dissolution or mineral reactions.

Even though these results do not allow to fully determine the cause and exact quantification of the significant change in failure potential, they have interesting implications for geo-engineering scenarios. These new results imply that a reservoir, after influx of chemically different fluids (for example due to use of enhanced recovery methods), can show a different mechanical response within days — whereas slow geological processes usually take on the order of centuries and millennia. The potential magnitude of the effect of pore fluid chemistry highlights that the field of fluid–rock interaction requires more study at all sample scales, in particular to improve understanding in geo-engineering settings as well as for natural hazards, especially earthquake mechanics.

CRediT authorship contribution statement

A. Pluymakers: Conceptualization, Funding acquisition, Methodology, Resources (experimental), Writing - original draft, Visualization, Writing - review & editing. **A. Ougier-Simonin:** Aided, Data curation (experimental), Funding acquisition, Methodology, Resources (experimental), Visualization, Writing - review & editing. **A. Barnhoorn:** Fine-tuning, Data curation (tomography), Methodology, Resources (microtomography), Visualization, Writing - review & editing.

Declaration of competing interest

The authors declare that they have no known competing financial interests or personal relationships that could have appeared to influence the work reported in this paper.

Acknowledgements

We thank Matt Kirkham for aiding the experimental work and Ellen Meijvogel-de Koning and Wim Verwaal for executing the micro-tomography scans. This paper has benefited from discussions with dr. Mike Heap, University of Strasbourg and prof. Chris Spiers, Utrecht University. We thank the Editor and all Reviewers for their comments which have improved the paper significantly. Funding comes from the Horizon 2020 Programme ECCSEL no. 675206 and the BGS Science Programme. A.P. is currently supported by the Dutch Foundation for Scientific Research (NWO) (No. 016.Veni.181.036). This paper is published with permission from the Executive Director of the British Geological Survey. All data is available in the manuscript and the supplementary materials; raw data is accessible at 10.4121/uuid:3ed61ee6-ce13-4792-af76-eS5226aeS3cc.

Appendix A. Supplementary data

Supplementary material related to this article can be found online at https://doi.org/10.1016/j.gete.2021.100233.

References

1. Kristiansen T, Barkved O, Landrø M, Amundsen L. Linking seismic response to geomechanics. *GEO ExPro*. 2009;6(6). Accessed March 7, 2019. https://www.geoexpro.com/articles/2009/06/linking-seismic-response-to-geomechanics.
2. Plummer LN, Busenberg E. The solubilities of calcite, aragonite and vaterite in CO2-H2O solutions between 0 and 90 °C, and an evaluation of the aqueous model for the system CaCO3-CO2-H2O. *Geochim Cosmochim Acta*. 1982;46(6):1011–1040. http://dx.doi.org/10.1016/0016-7037(82)90056-4.
3. Sjöberg EL, Rickard DT. Temperature dependence of calcite dissolution kinetics between 1 and 62 °C at pH 2.7 to 8.4 in aqueous solutions. *Geochim Cosmochim Acta*. 1984;48(3):485–493. http://dx.doi.org/10.1016/0016-7037(84)90276-X.
4. Pokrovsky OS, Golubev SV, Schott J. Dissolution kinetics of calcite, dolomite and magnesite at 25 °C and 0 to 50 atm pCO2. *Chem Geol*. 2005;217(3–4):239–255. http://dx.doi.org/10.1016/J.CHEMGEO.2004.12.012.
5. Atkinson BK. Subcritical crack propagation in rocks: theory, experimental results and applications. *J Struct Geol*. 1982;4(1):41–56.
6. Rutter E. Pressure solution in nature, theory and experiment. *J Geol Soc Lond*. 1983;140(5):725–740. http://dx.doi.org/10.1144/gsjgs.140.5.0725.
7. Ferguson G, McIntosh JC, Grasby SE, et al. The persistence of Brines in sedimentary basins. *Geophys Res Lett*. 2018;45(10):4851–4858. http://dx.doi.org/10.1029/2018GL078409.
8. Barnes I, Hem JD. Chemistry of subsurface waters. *Annu Rev Earth Planety Sci*. 1973;1:157–181. http://dx.doi.org/10.1146/annurev.ea.01.050173.001105.
9. Verberne BA, Spiers CJ, Niemeijer AR, De Bresser JHP, De Winter DAM, Plümper O. Frictional properties and microstructure of calcite-rich fault gouges sheared at sub-seismic sliding velocities. *Pure Appl Geophys*. 2013;171(10):2617–2640. http://dx.doi.org/10.1007/s00024-013-0760-0.
10. Miller SA, Collettini C, Chiaraluce L, Cocco M, Barchi M, Kaus BJP. Aftershocks driven by a highpressure CO2 source at depth. *Nature*. 2004;427(724–727).
11. Jansen G, Ruhl CJ, Miller SA. Fluid pressure triggered foreshock sequence of the 2008 Mogul earthquake sequence: Insights from stress inversion and numerical modeling. *J Geophys Res Solid Earth*. 2019. http://dx.doi.org/10.1029/2018JB015897, Published online March 12, 2019.
12. Fulton PM, Brodsky EE. In situ observations of earthquake-driven fluid pulses within the Japan Trench plate boundary fault zone. *Geology*. 2016;44(10):851–854. http://dx.doi.org/10.1130/G38034.1.
13. McClure M. Generation of large post-injection induced seismic events by backflow from dead-end faults and fractures. *Geophys Res Lett*. 2015. http://dx.doi.org/10.1002/2015GL065028, Published online 2015:n/a-n/a.
14. Guglielmi Y, Cappa F, Avouac J-P, Henry P, Elsworth D. Seismicity triggered by fluid injection-induced aseismic slip. *Science*. 2015;348(6240):1224–1226. http://dx.doi.org/10.1126/science.aab0476.
15. Shapiro SA, Dinske C. Fluid-induced seismicity: Pressure diffusion and hydraulic fracturing. *Geophys Prospect*. 2009;57(2):301–310. http://dx.doi.org/10.1111/j.1365-2478.2008.00770.x.
16. Barbour AJ, Pollitz F. Induced seismicity reduces Seismic Hazard?. *Geophys Res Lett*. 2019;46(8):4170–4173. http://dx.doi.org/10.1029/2019GL081991.
17. Lisabeth HP, Zhu W. Effect of temperature and pore fluid on the strength of porous limestone. *J Geophys Res B*. 2015;120(9):6191–6208. http://dx.doi.org/10.1002/2015JB012152.
18. Nicolas A, Fortin J, Regnet JB, Dimanov A, Guéguen Y. Brittle and semi-brittle behaviours of a carbonate rock: influence of water and temperature. *Geophys J Int*. 2016;206(1):438–456. http://dx.doi.org/10.1093/gji/ggw154.
19. Risnes R, Madland MV, Hole M, Kwabiah NK. Water weakening of chalk— Mechanical effects of water–glycol mixtures. *J Pet Sci Eng*. 2005;48:21–36, Accessed September 19, 2016. https://vpn2.uio.no/+CSCO+0h756767633A2F2F6A6A6A2E667076726170727176657270672E70627A++/science/article/pii/S0920410505000768.
20. Rutter E. The influence of temperature, strain rate, and intrastitial water in the experimental deformation of calcite rocks. *Tectonophysics*. 1974;22(3–4):311–334. http://dx.doi.org/10.1016/0040-1951(74)90089-4.
21. Baud P, Schubnel A, Heap M, Rolland A. Inelastic compaction in high-porosity limestone monitored using acoustic emissions. *J Geophys Res Solid Earth*. 2017;122(12). http://dx.doi.org/10.1002/2017JB014627, 9989-10, 008.
22. Risnes R, Haghighi H, Korsnes RI, Natvik O. Chalk-fluid interactions with glycol and brines. *Tectonophysics*. 2003;370(1–4):213–226. http://dx.doi.org/10.1016/S0040-1951(03)00187-2.
23. Megawati M, Hiorth A, Madland MV. The impact of surface charge on the mechanical behavior of high-porosity chalk. *Rock Mech Rock Eng*. 2013;46(5):1073–1090. http://dx.doi.org/10.1007/s00603-012-0317-z.
24. Heggheim T, Madland MV, Risnes R, Austad T. A chemical induced enhanced weakening of chalk by seawater. *J Pet Sci Eng*. 2005;46(3):171–184. http://dx.doi.org/10.1016/J.PETROL.2004.12.001.
25. Zhang X, Spiers CJ. Compaction of granular calcite by pressure solution at room temperature and effects of pore fluid chemistry. *Int J Rock Mech Min Sci*. 2005;42(7–8):950–960, http://www.sciencedirect.com/science/article/pii/S1365160905000754.
26. Bergsaker AS, Røyne A, Ougier-Simonin A, Aubry J, Renard F. The effect of fluid composition, salinity and acidity on subcritical crack growth in calcite crystals. *J Geophys Res Solid Earth*. 2016;121(3):1631–1651. http://dx.doi.org/10.1002/2015JB012723.
27. Wanner C, Eichinger F, Jahrfeld T, Diamond LW. Causes of abundant calcite scaling in geothermal wells in the Bavarian Molasse Basin, Southern Germany. *Geothermics*. 2017;70:324–338. http://dx.doi.org/10.1016/j.geothermics.2017.05.001.
28. Song J, Zeng Y, Wang L, et al. Surface complexation modeling of calcite zeta potential measurements in brines with mixed potential determining ions (Ca2+, CO32-, Mg2+, SO42-) for characterizing carbonate wettability. *J Colloid Interface Sci*. 2017;506:169–179. http://dx.doi.org/10.1016/J.JCIS.2017.06.096.
29. Pokrovsky OS, Schott J. Surface chemistry and dissolution kinetics of divalent metal carbonates. *Environ Sci Technol*. 2002;36(3):426–432. http://dx.doi.org/10.1021/es010925u.
30. Pluymakers A, Peach C, Spiers C. Diagenetic compaction experiments on simulated anhydrite fault gouge under static conditions. *J Geophys Res Solid Earth*. 2014;119(5):4123–4148. http://dx.doi.org/10.1002/2014JB011073.
31. Charlton SR, Parkhurst DL. Modules based on the geochemical model PHREEQC for use in scripting and programming languages. *Comput Geosci*. 2011;37(10):1653–1663. http://dx.doi.org/10.1016/j.cageo.2011.02.005.
32. Castagna A, Ougier-Simonin A, Benson PM, et al. Thermal damage and pore pressure effects on brittle-ductile transition of comiso limestone. *J Geophys Res Solid Earth*. 2018;123(9):7644–7660. http://dx.doi.org/10.1029/2017JB015105.
33. Bakker RR, Violay MES, Benson PM, Vinciguerra SC. Ductile flow in subvolcanic carbonate basement as the main control for edifice stability: New experimental insights. *Earth Planet Sci Lett*. 2015;430:533–541. http://dx.doi.org/10.1016/J.EPSL.2015.08.017.
34. Delle Piane C, Burlini L, Kunze K. The influence of dolomite on the plastic flow of calcite. Rheological, microstructural and chemical evolution during large strain torsion experiments. *Tectonophysics*. 2009;467(1–4):145–166. http://dx.doi.org/10.1016/j.tecto.2008.12.022.
35. Kushnir ARL, Kennedy LA, Misra S, Benson P, White JC. The mechanical and microstructural behaviour of calcite-dolomite composites: An experimental investigation. *J Struct Geol*. 2015;70:200–216. http://dx.doi.org/10.1016/j.jsg.2014.12.006.
36. Woodman J. Thermo-mechanical loading of intact rock and discontinuities. 2020 Published online 2020.
37. Okubo S, Nishimatsu Y. Uniaxial compression testing using a linear combination of stress and strain as the control variable. *Int J Rock Mech Min Sci Geomech Abstr*. 1985;22(5):323–330. http://dx.doi.org/10.1016/0148-9062(85)92064-9.
38. Wawersik WR, Fairhurst C. A study of brittle rock fracture in laboratory compression experiments. *Int J Rock Mech Min Sci Geomech Abstr*. 1970;7(5):561–575. http://dx.doi.org/10.1016/0148-9062(70)90007-0.
39. Hudson JA, Brown ET, Fairhurst C. Optimizing the control of rock failure in servo-controlled laboratory tests. *Rock Mech Felsmechan Méc Roches*. 1971;3(4):217–224. http://dx.doi.org/10.1007/BF01238181.

40. Hudson JA, Crouch SL, Fairhurst C. Soft, stiff and servo-controlled testing machines: a review with reference to rock failure. *Eng Geol*. 1972;6(3):155–189. http://dx.doi.org/10.1016/0013-7952(72)90001-4.
41. He C, Okubo S, Nishimatsu Y. A study of the class II behaviour of rock. *Rock Mech Rock Eng*. 1990;23(4):261–273. http://dx.doi.org/10.1007/BF01043307.
42. Paterson MS, Wong T. *Experimental Rock Deformation - the Brittle Field*. 2nd ed. Berlin Heidelberg: Springer; 2005.
43. Birch F. The velocity of compressional waves in rocks to 10 kilobars: 1. *J Geophys Res*. 1960;65(4):1083–1102. http://dx.doi.org/10.1029/jz065i004p01083.
44. Yin H. *Acoustic Velocity and Attenuation of Rocks: Isotropy, Intrinsic Anisotropy, and Stress Induced Anisotropy*. 1992 Published online 1992.
45. Lee MW. Velocity ratio and its application to predicting velocities. 2020 Accessed August 21, 2020. http://geology.cr.usgs.gov/pub/bulletins/b2197/.
46. Anselmetti FS, Eberli GP. Controls on sonic velocity in carbonates. *Pure Appl Geophys PAGEOPH*. 1993;141(2–4):287–323. http://dx.doi.org/10.1007/BF00998333.
47. Mavko G, Mukerji T, Dvorkin J. *The Rock Physics Handbook*. Cambridge University Press; 1998.
48. Simmons G, Brace WF. Comparison of static and dynamic measurements of compressibility of rocks. *J Geophys Res*. 1965;70(22):5649–5656. http://dx.doi.org/10.1029/jz070i022p05649.
49. Walsh JB. The effect of cracks on the uniaxial elastic compression of rocks. *J Geophys Res*. 1965;70(2):399–411. http://dx.doi.org/10.1029/jz070i002p00399.
50. Yale DP, Jamieson WHJ. Static and dynamic mechanical properties of carbonates - OnePetro. In: Nelson PP, Lauback SE, eds. *Rock Mechanics*. Balkema; 1994:463–471.
51. Fjær E. Static and dynamic moduli of a weak sandstone. In: *Geophysics, Vol. 74*. Society of Exploration Geophysicists; 2009. http://dx.doi.org/10.1190/1.3052113.
52. Nicksiar M, Martin CD. Evaluation of methods for determining crack initiation in compression tests on low-porosity rocks. *Rock Mech Rock Eng*. 2012;45(4):607–617. http://dx.doi.org/10.1007/s00603-012-0221-6.
53. Rutter EH. On the nomenclature of mode of failure transitions in rocks. *Tectonophysics*. 1986;122(3–4):381–387. http://dx.doi.org/10.1016/0040-1951(86)90153-8.
54. Wong T, David C, Zhu W. The transition from brittle faulting to cataclastic flow in porous sandstones: Mechanical deformation. *J Geophys Res Solid Earth*. 1997;102(B2):3009–3025. http://dx.doi.org/10.1029/96jb03281.
55. Vajdova V, Baud P, Wong T. Compaction, dilatancy, and failure in porous carbonate rocks. *J Geophys Res*. 2004;109(B5):B05204. http://dx.doi.org/10.1029/2003JB002508.
56. Pluymakers A, Kobchenko M, Renard F. How microfracture roughness can be used to distinguish between exhumed cracks and in-situ flow paths in shales. *J Struct Geol*. 2017;94:87–97. http://dx.doi.org/10.1016/j.jsg.2016.11.005.
57. Buades A, Coll B, Morel JM. Image denoising methods. A new nonlocal principle. *SIAM Rev*. 2010;52(1):113–147. http://dx.doi.org/10.1137/090773908.
58. Baud P, Exner U, Lommatzsch M, Reuschlé T, Wong T. Mechanical behavior, failure mode, and transport properties in a porous carbonate. *J Geophys Res Solid Earth*. 2017;122(9):7363–7387. http://dx.doi.org/10.1002/2017JB014060.
59. Zhu W, Baud P, Wong T. Micromechanics of cataclastic pore collapse in limestone. *J Geophys Res*. 2010;115(B4):B04405. http://dx.doi.org/10.1029/2009JB006610.
60. Baud P, Wong T, Zhu W. Effects of porosity and crack density on the compressive strength of rocks. *Int J Rock Mech Min Sci*. 2014;67:202–211. http://dx.doi.org/10.1016/J.IJRMMS.2013.08.031.
61. Baud P, Rolland A, Heap M, et al. Impact of stylolites on the mechanical strength of limestone. *Tectonophysics*. 2016;690:4–20. http://dx.doi.org/10.1016/J.TECTO.2016.03.004.
62. Vialle S, Vanorio T. Laboratory measurements of elastic properties of carbonate rocks during injection of reactive CO_2 -saturated water. *Geophys Res Lett*. 2011;38(1). http://dx.doi.org/10.1029/2010GL045606, n/a-n/a.
63. Dziadkowiec J, Javadi S, Bratvold JE, Nilsen O, Røyne A. Surface Forces Apparatus measurements of interactions between rough and reactive calcite surfaces. *Langmuir*. 2018. http://dx.doi.org/10.1021/acs.langmuir.8b00797, Published online May 28, 2018:acs.langmuir.8b00797.
64. Diao Y, Espinosa-Marzal RM. Effect of fluid chemistry on the interfacial composition, adhesion and frictional response of calcite single crystals – implications for injection-induced seismicity. *J Geophys Res Solid Earth*. 2019. http://dx.doi.org/10.1029/2018JB017252, Published online May 12, 2019:2018JB017252.
65. Javadi S, Røyne A. Adhesive forces between two cleaved calcite surfaces in NaCl solutions: The importance of ionic strength and normal loading. *J Colloid Interface Sci*. 2018;532:605–613. http://dx.doi.org/10.1016/j.jcis.2018.08.027.
66. Røyne A, Dalby KN, Hassenkam T. Repulsive hydration forces between calcite surfaces and their effect on the brittle strength of calcite bearing rocks. *Geophys Res Lett*. 2015;42(12):4786–4794. http://dx.doi.org/10.1002/2015GL064365.
67. Usdowski E. In: Purser BH, Tucker ME, Zenger DH, eds. *Dolomites: A Volume in Honour of Dolomieu*. Dolomites: A Volume in Honour of Dolomieu; 2009:464.
68. Busenberg E, Plummer LN. Thermodynamics of magnesian calcite solid-solutions at 25 °C and 1 atm total pressure. *Geochim Cosmochim Acta*. 1989;53(6):1189–1208. http://dx.doi.org/10.1016/0016-7037(89)90056-2.
69. Madland MV, Hiorth A, Omdal E, et al. Chemical alterations induced by rock–fluid interactions when injecting brines in high porosity Chalks. *Transp Porous Media*. 2011;87(3):679–702. http://dx.doi.org/10.1007/s11242-010-9708-3.
70. Korsnes RI, Strand S, Hoff O, Pedersen T, Madland MV, Austad T. Does the chemical interaction between seawater and chalk affect the mechanical properties of chalk?. In: Cottheim A, Charlier R, Thimus JF, Tshibangu JP, eds. *Multiphysics Coupling and Long Term Behaviour in Rock Mechanics*. 2006:427–434, Accessed February 1, 2019. https://books.google.nl/books?hl=nl&lr=&id=GFBsBgAAQBAJ&oi=fnd&pg=PA427&dq=Korsnes+R,+Strand+S,+Hoff,+Pedersen+T,+Madland+M,+Austad+T+(2006)+Does+the+chemical+interaction+between+seawater+and+chalk+affect+the+mechanical+properties+of+chalk%3F+In:+Cottheim.
71. Hong M, Xu J, Teng HH. Evolution of calcite growth morphology in the presence of magnesium: Implications for the dolomite problem. *Geochim Cosmochim Acta*. 2016;172:55–64. http://dx.doi.org/10.1016/J.GCA.2015.09.022.
72. Røyne A, Dalby KN, Hassenkam T. Repulsive hydration forces between calcite surfaces and their effect on the brittle strength of calcite-bearing rocks. *Geophys Res Lett*. 2015;42(12):4786–4794. http://dx.doi.org/10.1002/2015GL064365.